A method for applying lateral surface eddy diffusion in ocean models with a general vertical coordinate

Gustavo M. Marques[1], Andrew E. Shao[2], Scott D. Bachman[1], Gokhan Danabasoglu[1], Frank O. Bryan[1]

[1]Climate and Global Dynamics Laboratory, National Center for Atmospheric Research, Boulder, CO
[2]Canadian Centre for Climate Modelling and Analysis, Environment and Climate Change Canada, Victoria, BC Canada

Key Points:

- A method for applying lateral diffusion within the surface boundary layer of general vertical coordinate ocean models is proposed.
- Regridding/remapping techniques are used to represent tracers in a z-coordinate, where lateral fluxes are easily applied.
- The method reduces tracer biases in forced global simulations, regardless of the coordinate system employed.

Corresponding author: Gustavo Marques, gmarques@ucar.edu

Abstract

The mixing of tracers by mesoscale eddies, parameterized in many ocean general circulation models (OGCMs) as a diffusive process, contributes significantly to the distribution of tracers in the ocean. In the ocean interior, such processes occur mostly along the direction parallel to the local neutral density surface. However, near boundaries, small-scale turbulence breaks this constraint and the mesoscale transport occurs mostly along a plane parallel to the boundary (i.e., laterally near the surface of the ocean). Although this process is easily represented in OGCMs with geopotential vertical coordinates, the representation is more challenging in OGCMs that use a general vertical coordinate, where surfaces can be tilted with respect to the horizontal. We propose a method for representing the diffusive lateral mesoscale fluxes within the surface boundary layer of general vertical coordinate OGCMs. The method relies on regridding/remapping techniques to represent tracers in a geopotential grid. Lateral fluxes are calculated in this grid and then remapped back to the native grid, where fluxes are applied. The algorithm is implemented in an ocean model and tested in idealized and realistic settings. Lateral diffusion reduces the vertical stratification of the upper ocean, which results in an overall deepening of the surface boundary layer depth. Although the impact on certain global metrics is not significant, enabling lateral diffusion leads to small but meaningful reduction in the near-surface global bias of potential temperature and salinity.

Plain Language Summary

Mesoscale ocean eddies, which are analogous to the weather systems in the atmosphere, are crucial to the distribution of heat, salt, carbon, and nutrients throughout the global ocean. Most of the ocean models used in climate simulations do not have enough horizontal resolution to resolve these eddies and, therefore, their effects must be parameterized. Away from ocean boundaries, where no heat or mass is exchanged across ocean surfaces, the mixing of tracers due to mesoscale eddies occurs along surfaces of constant density. However, as ocean boundaries are approached, mixing then occurs in a plane parallel to the boundary. For example, near the surface of the ocean, which is where the scheme presented here is designed to work, this plane is mostly lateral. There is a class of ocean models that rely on a vertical coordinate system whose layer thicknesses can vary in the horizontal, thus complicating the implementation of lateral diffusive param-

eterizations. This paper presents and evaluates a method that allows lateral fluxes to be calculated and applied in this class of ocean models.

1 Introduction

Mesoscale eddies contain most of the oceanic kinetic energy and play a key role in distributing heat, salt, carbon, and other tracers throughout the world's oceans. Based on the results of numerical simulations, it is now recognized that mesoscale eddies are an important component of the Earth's climate system (Hallberg & Gnanadesikan, 2006; Farneti et al., 2010; Marshall et al., 2017; Griffies et al., 2015). Despite recent advances in compute power, horizontal resolutions of the ocean models used in multi-century climate projections (i.e., models that are used for the Intergovernmental Panel on Climate Change) are not enough to explicitly resolve mesoscale eddies everywhere. Therefore, these models must rely on mesoscale eddy parameterizations (i.e., Redi, 1982; Gent & McWilliams, 1990) that attempt to represent the effect of eddies in the ocean. Climate-relevant ocean metrics, such as mixed layer depth, and the uptake and transport of heat, are affected by details on the formulation of these parameterizations (i.e., Danabasoglu et al., 1994; Gnanadesikan et al., 2007; Danabasoglu et al., 2008; Urakawa et al., 2020).

The most prevalent mesoscale eddy parameterizations generally consist of two parts: 1) eddy-diffusive transport, where tracers are diffused along isopycnal surfaces (or surfaces of constant neutral density) using a down-gradient approach (Solomon, 1971; Redi, 1982); and 2) eddy-advective transport, where an additional advection of tracers by the eddy-induced velocity acts to flatten isopycnals, thereby reducing potential energy (Gent & McWilliams, 1990; Gent et al., 1995; Griffies, 1998). Away from boundaries, both the eddy-diffusive and eddy-advective transports are nearly aligned with neutral density surfaces. However, as argued by Tréguier et al. (1997) and Ferrari et al. (2008, 2010), when eddies approach the surface the presence of the atmospheric boundary requires that their advective and diffusive tracer fluxes become parallel to the surface rather than parallel to neutral directions.

In the surface and bottom boundary layers vigorous microscale turbulence is induced by a number of processes, including breaking surface and internal waves, destabilizing buoyancy fluxes (e.g., Taylor & Ferrari, 2010), and boundary stresses (e.g., Thomas, 2005; Thomas & Ferrari, 2008). The resultant mixing of the boundary layer stratifica-

tion increases the near-surface isopycnal slopes, which in conjunction with frontogenetic processes (e.g., Hoskins, 1982; Gula et al., 2014) leads to frequent outcropping of density surfaces. It is thus natural to conclude that the framework of parameterizing eddy fluxes along density surfaces must break down in the boundary layers to avoid fluxing tracers through the vertical boundaries. Rather, the typical conception is that the fluxes are governed by geostrophic motions that are constrained to flow parallel to the boundary, i.e., in a purely horizontal direction near the surface and along bathymetric contours near the bottom (e.g., Ferrari et al., 2008).

Methods for tapering and tilting near-surface eddy transport have been developed in previous literature. First, Ferrari et al. (2008) derived a new eddy parameterization where the diabatic nature of the eddy fluxes could be retained near ocean boundaries. In this parameterization, eddy-induced velocity and diffusion are set parallel to the boundary within the turbulent boundary layer, while in the ocean interior eddy fluxes still occur along neutral planes. The two regimes are matched in the so-called transition layer, where the fluxes are progressively tilted from aligning with the neutral slope to being purely horizontal. This method was implemented and tested in a climate model, leading to improvements in the solution when compared to the results using the tapering approach (Danabasoglu et al., 2008).

Following Ferrari et al. (2008) and Danabasoglu et al. (2008), imposition of near-surface eddy fluxes across neutral planes is now a common practice in ocean general circulation models (OGCMs) with geopotential vertical coordinates, where horizontal becomes synonymous with along-layer, such as the Parallel Ocean Program version 2 (POP2; Danabasoglu et al., 2012), the Modular Ocean Model versions 4 and 5 (MOM4 and MOM5; Griffies et al., 2005; Griffies, 2012), and the Finite-element/volume Sea ice-Ocean Model version 1.4 (FESOM; Wang et al., 2014). In these models the transition from adiabatic to diabatic eddy fluxes is handled by a near-boundary eddy flux parameterization (Ferrari et al., 2008; Danabasoglu et al., 2008). This approach has thus become a fundamental element of coupled Earth system models that use these OGCMs. However, the recent trend toward OGCMs with general (or Lagrangian) vertical coordinates, such as the Modular Ocean Model version 6 (MOM6; Adcroft et al., 2019) and the ocean component of the Model for Prediction Across Scales (MPAS-O; Petersen et al., 2018), makes a similar implementation of diabatic near-surface eddy fluxes much more complex because the coordinate surfaces can be tilted with respect to the horizontal, and this tilt is determined

dynamically and evolves in time. Although applying neutral diffusion in such models is also non-trivial, recently Shao et al. (2020) have developed a neutral diffusion operator that is appropriate to this class of OGCMs. Therefore, only the lateral diffusive part remains missing.

To fill this gap, we present a method for applying lateral diffusive tracer fluxes due to mesoscale eddies within the surface boundary layer of general vertical coordinate ocean models. To make the method applicable to climate studies, we assure that it obeys the following requirements: (i) conservation of the total tracer content; (ii) tracer monotonicity (i.e., it does not create new tracer extremes); and (iii) it does not lead to a significant increase in the computational cost.

This manuscript is organized as follows. A description of the method is presented in Section 2. In Section 3 we use an idealized test case to provide a proof of concept of how this method operates in conjunction with the neutral diffusion scheme developed by Shao et al. (2020). In Section 4 we explore the effects of including surface lateral diffusion in global forced ocean–sea-ice simulations configured using two different coordinate systems and run via the Community Earth System Model (CESM) framework. Summary and discussion are given in section 5.

2 Description of the method

In this section we present an algorithm for applying lateral eddy diffusion in the surface boundary layer in models using Lagrangian vertical coordinates. This algorithm accounts for the effects of mesoscale diffusive fluxes whose direction is constrained by the geometry of the ocean surface. That is, unlike eddy fluxes in the ocean interior that are applied along neutral density surfaces, the following method imposes fluxes that are purely horizontal.

We will denote the parameterized diffusive flux of an arbitrary tracer ϕ as

$$\mathbf{F_L} = -\mathbf{K_L} \cdot \nabla\phi \tag{1}$$

where ϕ represents an averaged tracer. The nature of the averaging is not crucial for describing the method and is purposely left unspecific here; we only require that the average is taken over sufficiently many samples of ϕ that it converges statistically (i.e., adding

another sample will not meaningfully change the average). The parameterized flux is directed down the mean gradient of ϕ using a symmetric diffusion tensor, $\mathbf{K_L}$, and the fluxes are set to be purely lateral by choosing

$$\mathbf{K_L} = \kappa_L(x, y, z, t) \begin{pmatrix} 1 & 0 & 0 \\ 0 & 1 & 0 \\ 0 & 0 & 0 \end{pmatrix}, \tag{2}$$

where x, y, and z are the zonal, meridional and vertical (positive upward) directions, respectively, t is time, and $\kappa_L(x, y, z, t)$ is an user-specified scalar diffusion coefficient that varies in time and space. Note that $\mathbf{K_L}$ is equivalent to the Redi (1982) tensor in the limit where the neutral slopes are zero and there is no dianeutral flux. For simplicity of presentation we will assume an isotropic diffusion that is directed along the model coordinates; a more general, anisotropic prescription would replace κ_L and the identity matrix in the upper left minor of $\mathbf{K_L}$ with a symmetric matrix consisting of unequal diffusivities (Smith, 1999; Bachman et al., 2020).

Given that layer thicknesses can vary between two laterally adjacent cells in a Lagrangian vertical coordinate model, diffusing the tracer along layers is not enough to ensure that the flux is strictly horizontal. The method we propose to overcome this issue uses regridding/remapping techniques before applying the lateral fluxes, which is explained below.

2.1 Step 1: regridding/remapping

The first step is to define a new vertical grid, which we refer to as the LBD (Lateral Boundary Diffusion) grid hereafter, using layer interfaces from the native vertical grid, the boundary layer depth (BLD), and the maximum depth (H) from two adjacent water columns (Fig. 1a). In this manuscript BLD follows the definition given in the K-profile parameterization (KPP) for vertical mixing (Large et al., 1994), which is based on a critical Richardson number value. However, any other reasonable depth (e.g., mixed layer depth or BLD from a different vertical mixing scheme) can be used instead. Using the above-mentioned information, a geopotential vertical grid is constructed by combining layer thicknesses (h) and BLDs from both columns, starting at $z = 0$ (Fig. 1b).

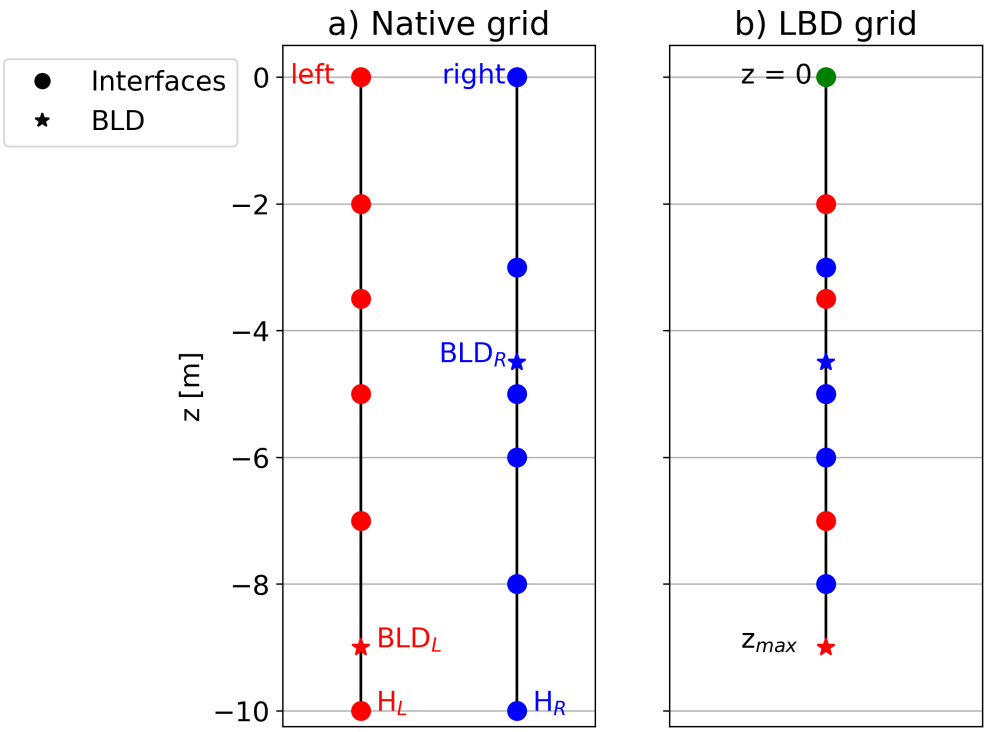

Figure 1. Demonstration of how the LBD grid is constructed. a) Layer interfaces (circles) and boundary layer depths (BLDs, stars) from two adjacent water columns (represented in red and blue). b) An example of the LBD grid, which is constructed by combining the distance between interfaces (i.e., layer thicknesses) and the boundary layer depths from both profiles shown in a). The first interface in the LBD grid is set to z=0 (green circle) and the last interface (z_{max}) is calculated using BLD_L, BLD_R, and the maximum depth of the left and right columns (H_L and H_R, respectively). See Eq. 3 for additional details on how to compute z_{max}.

Duplicated interface values are removed and the maximum depth (z_{max}) in the LBD grid is set to

$$z_{max} = \min\left(BLD_{max}, H_{min}\right), \tag{3}$$

where the subscripts L and R refer to the left and right columns, respectively, $BLD_{max} = \max\left(BLD_L, BLD_R\right)$ is the deeper BLD of the two columns, and $H_{min} = \min\left(H_L, H_R\right)$ is the shallower total depth. The LBD grid has enough resolution to correctly represent tracer concentrations in both columns as well as the tracer fluxes (at velocity points) between the two columns. It is not possible to define a unique LBD grid that works glob-

ally without relying on a prohibitively large (i.e., computational expensive) number of vertical points. Therefore, we have opted to define a new LBD grid for each pair of water columns and the procedure is repeated for each tracer and at every tracer time step.

Once the LBD grid is defined, tracer profiles from each neighboring cell are remapped onto this grid using a remapping scheme. The remapping must be both conservative and monotonic. Conservative remapping is necessary to preserve the integrated value of scalar concentration within machine precision. This is particularly important for long-duration climate simulations running for centuries or millennia, where the accumulation of spurious tracer content can meaningfully influence the solution. Monotonic remapping assures that no overshoots or new extrema are created. This is crucial for ocean variables that must be bounded (e.g., seawater salinity) since the lack of monotonicity can lead to undesirable effects, such as triggering nonphysical convective adjustments. The reader is referred to White and Adcroft (2008) for an overall description of high-order remapping schemes, including the piecewise parabolic method used throughout this manuscript. Note that, once the tracer is remapped to the LBD grid, "lateral" becomes synonymous with "layer-wise", and correctly orienting the diffusive fluxes becomes much more straightforward.

2.2 Step 2: Compute fluxes

Figure 2 shows two adjacent water columns where the tracer field has been remapped to the LBD grid shown in Fig. 1. This figure is used to describe the steps listed below.

2.2.1 Find vertical indices containing the boundary layer depths

A key priority is to ensure that the lateral diffusion in the boundary layer tapers smoothly to neutral diffusion in the ocean interior, with the transition point occurring at the shallowest BLD. To this end, the first step in this part of the algorithm is to find the vertical indices of the layers containing the BLD in both columns. For the scenarios shown in Fig. 2, these are k = 9 and 4 for the left and right columns, respectively. These vertical indices are then compared and the minimum (k_{min}) and maximum (k_{max}) indices are identified. For the scenario shown in Fig. 2, $k_{min} = 4$ and $k_{max} = 9$. Note that, by definition, k_{max} is always the vertical index of the deepest layer in the LBD grid. Between k_{min} and k_{max} we impose a transition zone where the strength of the lateral

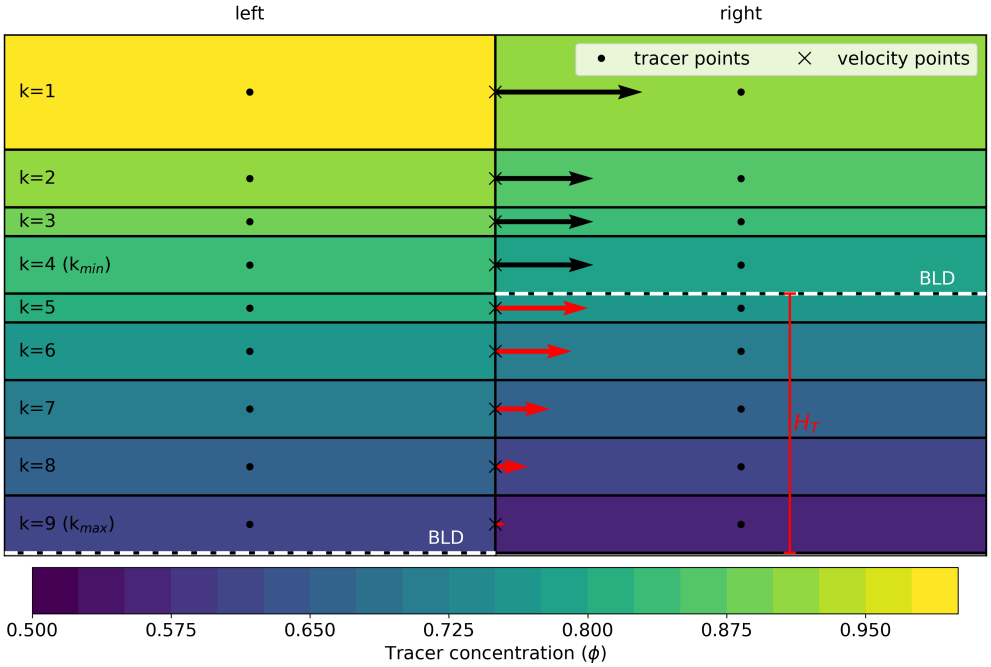

Figure 2. Tracer concentration (ϕ) in two adjacent water columns (left and right). The vertical grid is the example LBD grid shown in Fig. 1b, which has nine vertical levels (k). The dashed lines represent the boundary layer depth (BLD), while arrows represent the diffusive tracer fluxes computed at velocity points, with black (red) arrows indicating the surface (transition) zone. A linear decay in the fluxes is applied over the vertical extent of transition layer (H_T) , which is dictated by the bottom interface of layer indices k_{min} and k_{max}.

fluxes is gradually tapered to zero as one moves downward (toward larger k). Figure 2 shows the presence of a transition layer, but this layer can be absent in certain situations (e.g., when the BLD is the same in both columns, i.e. when $\mathrm{k}_{min} = \mathrm{k}_{max}$).

2.2.2 Compute fluxes at each layer

For each vertical layer index k, the diffusive flux (here presented for the zonal direction, with a meridional flux obtained analogously) is calculated at the interface between the two columns as

$$F_x(k) = -\kappa_L \; \Delta t \; h(k) \; \left[\phi_R(k) - \phi_L(k)\right] \frac{\Delta y}{\Delta x}, \tag{4}$$

where Δt is the tracer time step, $h(k)$ is the layer thickness, $\phi_R(k)$ and $\phi_L(k)$ are tracer concentrations on the right and left cells, respectively, and Δx and Δy are the width of the tracer cell in the zonal and meridional directions, respectively. Fluxes are calculated for each layer beginning at the surface layer ($k = 1$) and ending at the layer bounded by the shallowest BLD ($k = k_{min}$). This is illustrated by the black arrows in Fig. 2. Note that, assuming $\kappa_L > 0$, the diffusive fluxes are always layerwise down-gradient.

2.2.3 Taper the fluxes in the transition layer

If there is a transition layer, i.e., $\mathrm{k}_{max} > (\mathrm{k}_{min} + 1)$, the diffusive flux decays linearly between k_{min} and k_{max}. In this zone, Eq. 4 becomes

$$FT_x(k) = \alpha \; F_x(k) \quad \text{for } k > k_{min}, \tag{5}$$

where $FT_x(k)$ is the the diffusive flux in the transition layer. The nondimensional tapering coefficient α is

$$\alpha = H_T^{-1} \; [z + BLD_{min}] + 1, \tag{6}$$

where H_T is the distance between the bottom interfaces of the layers with indices k_{min} and k_{max}, z is the mean depth of the layer (the depth of the tracer point), and $BLD_{min} = \min(BLD_L, BLD_R)$. The linear decay imposed in Eq. 5 ensures that the fluxes are at full strength at $z = -BLD_{min}$ and become zero at $z = -(BLD_{min} + H_T)$. An example of how fluxes decay in the transition zone is shown by the red arrows in Fig. 2.

2.3 Remap fluxes onto the native grid

At this point in the algorithm, the thickness-weighted fluxes calculated in Section 2.2 must be transferred onto the model's native vertical coordinate. These fluxes are vertically extensive quantities (i.e., a quantity that is already volume weighted with respect to the vertical axis) and so the regridding/remapping approach used to transform the vertically intensive tracer concentrations is no longer appropriate. Instead, we apply a one dimensional conservative remapping that ensures that vertical integrals with the same depth extent are conserved between the two vertical coordinates. From now on we follow the convention that $(\cdot)$ represents the function specific to the model's native coor-

dinate and variables without the dot represent the function in the LBD coordinate. A thickness-weighted flux is constant between the interfaces of the discretized vertical grid and so this constraint is satisfied by a simple binning approach

$$\dot{F}_n = \sum_k a_k F_k, \tag{7}$$

where $\dot{F}_n$ is the thickness-weighted diffusive flux on layer n on the model's native grid, k is a layer index on the LBD grid, a_k is the fraction of that layer which falls within the depth range spanned by layer n, and F_k is the diffusive flux on the LBD grid. This method only has first-order accuracy, but seems to be sufficient in practice (see the experiments in section 3). Higher order methods can be constructed by adding additional integral constraints (e.g., a smoothness criterion based on vertical gradients).

In this procedure, the target layers in the destination grid are the layer thicknesses at cell interfaces, which is where fluxes are computed. To avoid non-zero fluxes in the presence of vanished layers, the layer thicknesses at cell interfaces are computed using the harmonic mean of two neighbouring thicknesses at tracer points. Once the fluxes are remapped to the target grid, a flux limiter must be applied to avoid up-gradient fluxes and maintain monotonicity. To do so, the maximum diffusive flux between two cells ($\dot{F}_{max}$) is calculated as

$$\dot{F}_{max}(k) = -c[(\dot{\phi}_R(k)\ \dot{V}_R(k)) - (\dot{\phi}_L(k)\ \dot{V}_L(k))], \tag{8}$$

where $\dot{V}_L(k)$ and $\dot{V}_R(k)$ are the volume of the left and right cells at vertical level k, respectively. The non-dimensional constant c is set to 0.2 in the simulations shown in sections 3 and 4, which represents the maximum fraction of the tracer concentration that can be isotropically diffused to each neighboring cell. That is, if a cell has an initial concentration of one and this cell is connected to four neighbouring cells with zero initial tracer concentration, the final (i.e., after steady state) tracer concentration in all cells will be 0.2. The diffusive flux is then limited as follows:

- If $\dot{F}_x \times \dot{F}_{max} < 0$, $\dot{F}_x = 0$;
- If $\dot{F}_x \times \dot{F}_{max} > 0$ and $\dot{F}_x > \dot{F}_{max}$, $\dot{F}_x = \dot{F}_{max}$;
- If $\dot{F}_x \times \dot{F}_{max} > 0$ and $\dot{F}_x < \dot{F}_{max}$, $\dot{F}_x$ is not modified.

The last step is to add the diffusive fluxes to the tracer tendency and iterate forward in time.

2.4 Summary of algorithm and additional remarks

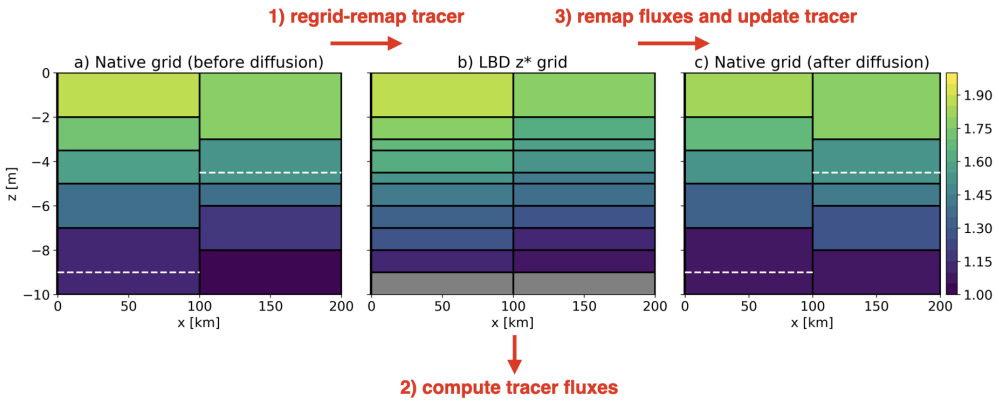

Figure 3. Schematic summarizing the main steps in the lateral diffusion algorithm (see text for details). The tracer concentration is represented by the colorbar in panel c).

The main steps are depicted in Fig. 3. The algorithm starts with the tracer concentration in a pair of water columns on the native model grid (Fig. 3a). The first step is to construct the LBD grid using layer thicknesses and the boundary layer depths from both columns, and then remap the initial tracer concentration onto this grid (Fig. 3b). The lateral tracer fluxes are computed on this grid by simply calculating the diffusive fluxes within each layer according to Eq. 4. These fluxes are then remapped to the velocity points on the native grid. After applying a flux limiter following Eq. 8, the fluxes are added to the tracer tendencies at each point and the tracer field is iterated forward in time. This procedure is repeated for every pair of water columns in both zonal and meridional directions and at every tracer time step.

3 Proof of concept using idealized simulations

The algorithm presented in section 2 is implemented in MOM6 (Adcroft et al., 2019), which uses a vertical Lagrangian-remap algorithm that enables general vertical coordinates (see section 4.1 for additional details about this model). To show how the algorithm described in the previous section works in practice, we consider a simple set of idealized experiments. These experiments do not include dynamics and only neutral and

lateral diffusion are applied to the tracers (i.e., advection and vertical diffusion are turned off). The neutral diffusion algorithm is described in Shao et al. (2020), and it is modified here to only act below z_{max}. Both, lateral and neutral diffusion coefficients are set to 1000 m^2 s^{-1}.

The horizontal domain is 200 × 100 km in the x and y directions, respectively, and with a constant grid spacing $\Delta x = \Delta y = 100$ km. The east and west boundaries are closed and the north and south boundaries are periodic. The ocean bottom is flat and the maximum depth (H_{max}) is 500 m. The initial potential temperature field, $\theta(z, x)$, is defined as

$$\theta(z, x) = \frac{\Delta\theta}{H_{max}} z + \theta_{surf}(x), \tag{9}$$

where z is the vertical direction and $\Delta\theta = 15\ ^oC$. A zonal gradient is imposed by setting $\theta_{surf}(x) = 20\ ^oC$ at x = 50 km and $\theta_{surf}(x) = 19\ ^oC$ at x = 150 km. We also define a salinity field, $S(z)$, which acts as a passive tracer and only varies vertically:

$$S(z) = -\frac{\Delta S}{H_{max}} z + S_{surf}, \tag{10}$$

where $\Delta S = 1$ ppt and $S_{surf} = 35$ ppt. The initial conditions for both θ and S are shown in Figs. 4a,b, respectively.

A linear equation of state is applied so that

$$\rho = \rho_0 + \partial_\theta \rho\ \theta, \tag{11}$$

where ρ is the *in situ* density, $\rho_0 = 1035$ kg m^{-3} is the reference density, and $\partial_\theta \rho$ = -0.255 kg m^{-3} °C^{-1}. This leads to a constant isopycnal slope of 3.3 ×10^{-4} everywhere (Fig. 4a).

Analysis of θ and S can be used to isolate the effects of neutral diffusion from those due to lateral diffusion. Since ρ is only a function of θ, only lateral diffusion should act on θ. Similarly, $\partial_x S = 0$ so only neutral diffusion should affect S. To quantify and visualize the effects of both neutral and lateral diffusion on the same tracer, we add a sec-

ond passive tracer τ that does not vary with depth and has a horizontal gradient of $\partial_x \tau$ = 0.01 km^{-1}.

Because the lateral diffusion scheme acts only within the BLD, we artificially set BLD to 100 m at x = 50 km and 300 m at x = 150 km (Fig. 4b). This configuration gives a surface zone ($z > -100$ m) where only lateral diffusion is applied, a transition zone ($-300 < z < -100$ m) where the lateral diffusion decays linearly, and an interior adiabatic zone ($z \leq -300$ m) where only neutral diffusion is applied.

Two experiments are conducted (LBD-Z and LBD-H) that differ only in terms of the vertical coordinate system employed. For experiment LBD-Z, a z* coordinate (Stacey et al., 1995; Adcroft & Campin, 2004) is chosen with a total of 50 equally spaced vertical layers (Δz = 10 m). For experiment LBD-H, a hybrid depth-isopycnal vertical coordinate motivated by Bleck (2002) and following Adcroft et al. (2019) is employed using a total of 25 layers. This coordinate behaves like z* down to $z \sim$ -40 m (with $\Delta z \sim$ 9 m), and then it transitions to a density based coordinate below that, where $\Delta\rho$ between two layer interfaces is always 0.192 kg m^{-3}, leading to the layer thicknesses shown in Fig. 4c. Notice that the left and right columns have different thicknesses below z $\sim$ -40 m.

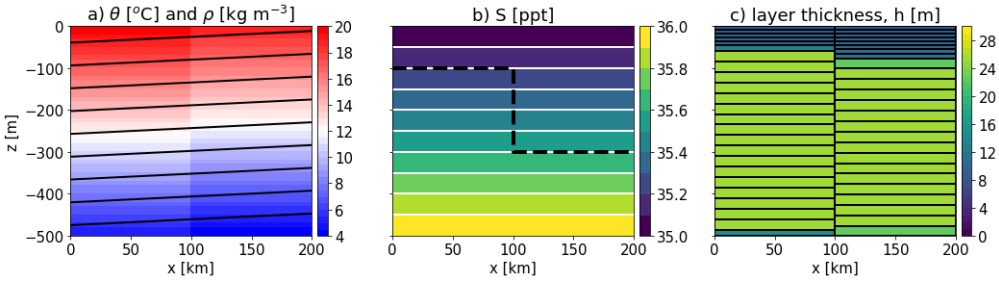

Figure 4. Initial conditions used in the idealized simulations. a) potential temperature (θ, °C), with black contours showing isopycnals where the top density contour is 22.0 kg m^{-3} with an increment of 5.0 kg m^{-3}; b) salinity (S, ppt), with white contours showing S every 0.1 ppt. The black dashed line shows the imposed boundary layer depth. c) layer thicknesses (h, m) in the LBD-H experiment, with the black contours highlighting the tracer cells in both columns.

We now evaluate tendency profiles due to lateral and neutral diffusion after one tracer time step (Δt = 1800 s). These profiles are taken at x = 50 and 150 km.

Figure 5a shows the tendency in θ from lateral diffusion in both experiments. In LBD-Z, the left and right tendencies are symmetric, because layer thicknesses do not vary horizontally in the z* grid. On the other hand, with the exception of a region where the grid behaves like a z* grid (e.g., the first $\sim$ 40 m), the profiles in LBD-H are mostly asymmetric because layer thicknesses vary horizontally in this case. In both experiments the tendency in θ from lateral diffusion decays linearly within the transition zone and then vanishes below the deepest BLD (z = -300 m). By design, the tendency in θ from neutral diffusion is zero throughout the entire water column in both experiments (Fig. 5b). Similarly, the tendency in S from lateral diffusion is also zero everywhere (Fig. 5c). This is despite the fact that in the LBD-H experiment S can vary horizontally for a fixed vertical index because thicknesses are not the same in the left and right columns. However, diffusive fluxes are computed after the tracers are remapped to the LBD grid, where $\partial_x S = 0$.

The tendency in S from neutral diffusion is shown in Fig. 5d. Notice that the right column in LBD-H (red line) has a non-zero value within the transition zone. This is because the BLD falls within this layer and, therefore, neutral diffusion fluxes can still be applied there. Lastly, the tendencies in τ from lateral and neutral diffusion are shown in Figs. 5e and f, respectively. Regardless of the coordinate system, the combined effects of lateral and neutral diffusion always leads to one point in each column where both schemes give zero tendencies (see region where -300 m $<$ z $<$ - 270 m in Figs. 5e and f; notice that some of these points overlap on each other). This is a limitation of our method and we discuss this further in Section 5.

4 Effects on global forced simulations

4.1 Model descriptions

Global simulations are performed using the Community Earth System Model version 2 (CESM2) framework (Danabasoglu et al., 2020) with active ocean and sea-ice components.

The ocean model is MOM6 (Adcroft et al., 2019), which is the same model used in Section 3. MOM6 has been selected as the new ocean model component for the upcoming versions of CESM. It uses an Arbitrary-Lagrangian-Eulerian (ALE) algorithm in the vertical, which allows application of any vertical coordinate system (e.g., geo-potential,

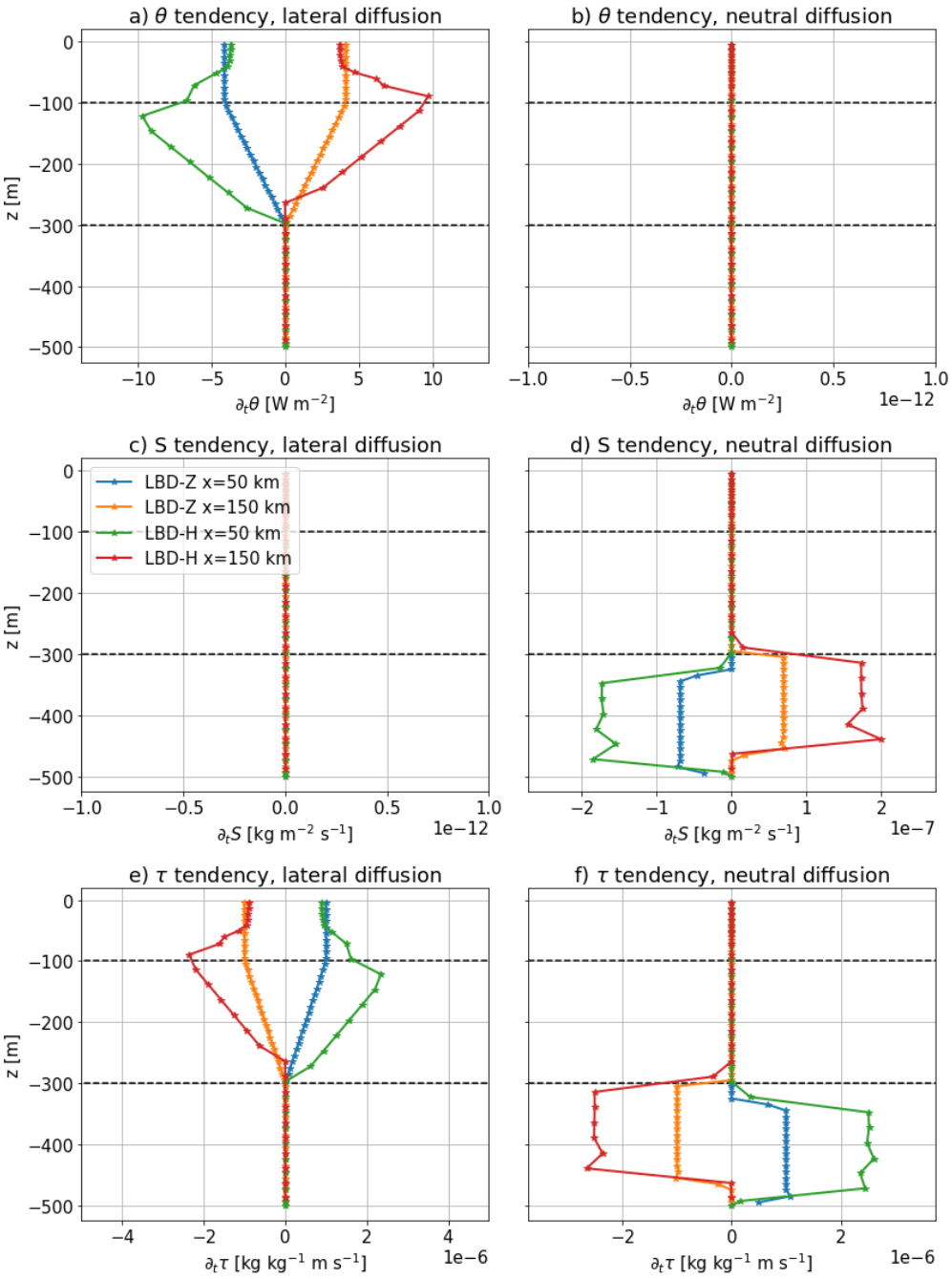

Figure 5. Profiles of tracer tendencies taken at two adjacent points (x = 50 and 150 km) and after one tracer time step. Results from two experiments (LBD-Z and LBD-H) are shown. a) θ tendency due to lateral diffusion; b) θ tendency due to neutral diffusion; c) S tendency due to lateral diffusion; d) S tendency due to neutral diffusion; e) τ tendency due to lateral diffusion; and f) τ tendency due to neutral diffusion. Black dashed line highlights the transition zone.

isopycnal, terrain-following, or any combination of them). Errors due to remapping are minimized via high-order accurate reconstructions (White & Adcroft, 2008; White et al., 2009). Unless otherwise stated, MOM6's dynamical core has been configured following Adcroft et al. (2019). A brief description of the sub-gridscale parameterizations employed in the present study is provided below. We attempt to keep these parameterizations and their settings as close as possible to what has been used in recent applications of the POP2 model within CESM (e.g., Danabasoglu et al., 2020; Tsujino et al., 2020). We emphasize that the parameters and choice of physics in MOM6 for CESM is a moving target and, therefore, the description below reflects the configuration employed when the experiments presented here were conducted.

The KPP parameterization for vertical mixing (Large et al., 1994) is incorporated via the Community ocean Vertical Mixing (CVMix) framework. In addition to accounting for the mixing in the surface boundary layer, KPP is also used to represent the vertical mixing in the ocean interior due to convection, double-diffusion, and vertical shear of the horizontal velocity. The latitude-dependent diffusivity due to internal wave mixing defined in Danabasoglu et al. (2012) is included, with a background vertical diffusivity of 2×10^{-5} m^2 s^{-1}. Energy dissipation from tidally-induced breaking internal gravity waves is represented using the scheme developed by Simmons et al. (2004).

The restratifying effects of baroclinic eddies in the mixed layer are represented using the parameterization developed by Fox-Kemper et al. (2008) as implemented by Fox-Kemper et al. (2011). The MOM6 implementation of this scheme has been modified as described in Adcroft et al. (2019). We set the frontal length scale to 1 km and the efficiency coefficient to 0.0625. The mixed layer depth (MLD) used in this scheme is calculated via the 0.03 kg m^{-3} potential density criteria. To ensure that restratification of the deepest mixed layer is persistent, a running-mean filter with a time scale of 5 days is applied to the MLD.

In addition to the near-surface lateral eddy diffusion scheme that is the focus of this manuscript, mesoscale eddies are represented by activating two additional schemes in the tracer equation. The first scheme follows the ideas of Gent and McWilliams (1990), where available potential energy is removed from the large scale by flattening isopycnals (hereafter GM). This scheme is implemented using the stream function formulation of Ferrari et al. (2010). By following what is commonly done in layer models (e.g., Bleck,

2002), the associated eddy-induced transport is applied as a bolus velocity. To avoid the problems associated with layer thickness diffusion described by Holloway (1997), the scheme is implemented as an interface height diffusion. The second scheme applies the diffusive mixing of tracers along neutral directions following the idea of Solomon (1971) and Redi (1982). The implementation of the neutral diffusion algorithm in MOM6 is described in Shao et al. (2020) and we chose the continuous reconstruction option for the present study. As mentioned in Section 3, we have modified this scheme to act only below the surface boundary layer.

The mesoscale eddy diffusivities are prescribed using a prognostic equation for the mesoscale eddy kinetic energy (hereafter MEKE; Jansen et al., 2015), the values for which are then fed into an expression relating it to the diffusivity. The expression we use is based on the geometric formalism of Marshall et al. (2012), except that we employ the eddy kinetic energy instead of the full (kinetic plus potential) eddy energy. The MEKE field is initialized by assuming the eddy kinetic energy budget is in an instantaneous balance between the bottom friction and the baroclinic source terms (eqs. 2 and 3 in Jansen et al. (2015)), which yields a simple algebraic expression for the eddy kinetic energy that is based on the stratification parameters and bottom drag coefficient. The MEKE prognostic equation is then iterated forward in time to predict the evolution of the eddy kinetic energy and hence the diffusivity. The same two-dimensional diffusivity field is used by the neutral and lateral diffusion schemes. This is also the surface diffusivity field used in the GM parameterization, but in this case a vertical structure on the diffusivity is imposed based on the equivalent barotropic mode (Adcroft et al., 2019).

Viscous terms are added to the horizontal momentum equation using both Laplacian and biharmonic operators with coefficients set via the MEKE scheme. Momentum is extracted via a quadratic drag law with a constant bottom friction coefficient $C_d = 3 \times 10^{-3}$. The non-linear equation of state for sea water defined by (Wright, 1997) is applied.

The sea-ice component is CICE Version 5.1.2 (CICE5; Bailey et al., 2018), with the improvements listed in Danabasoglu et al. (2020). With the exception of the horizontal grid, CICE5 has been configured following the description for the CESM-POP model provided in Tsujino et al. (2020).

4.2 Experimental design

The four global forced simulations conducted here are summarized in Table 1. They differ in terms of the vertical coordinate system (hybrid or z*, the same coordinates employed in Section 3), number of vertical layers (NK), whether neutral diffusion is applied throughout the entire water column or just below BLD_{max}, and whether the lateral diffusion scheme is enabled. The z* vertical coordinate has 65 layers with Δz = 2.5 m down to z = -10 m. The vertical resolution follows a hyperbolic tangent function where Δz increases to 250 m at $z \sim$ -3000 m, remaining constant until the bottom is reached. The hybrid vertical coordinate has 41 layers and is a combination of z* near the surface and potential density (referenced to 2000 dbar) elsewhere. The depth of transition between z* to isopycnal is shallowest in the tropics ($\sim$ 50 m) and deepens toward high latitudes ($\sim$ 1200 and 2000 m in the Southern and Northern Hemispheres, respectively).

The simulations start from rest and the initial potential temperature and salinity fields are derived from the January-mean climatology of the World Ocean Atlas 2018 (WOA18; Locarnini et al., 2018; Zweng et al., 2019). The sea surface salinity is restored to the monthly climatology of the upper 10-m averaged salinity from WOA18 using a piston velocity = 0.1667 m/day.

Both the sea-ice and ocean models share the same tripolar horizontal grid with a nominal resolution of 2/3 ° and equatorial refinement of 1/4 °. Bottom topography and coastlines are derived from the ETOPO1 dataset. The minimum and maximum depth are set to 10 m and 6000 m, respectively.

The simulations are forced using the JRA55-do v1.3 dataset (Tsujino et al., 2018) and the total integration time is one forcing cycle (1958–2016; total of 58 years). Unless otherwise stated, the results presented in the next section have been averaged over the last 30 years of the run.

4.3 Results

In this section, we compare the simulations listed in Table 1 focusing on the impact of the lateral diffusion scheme outlined in Section 2 on climate-relevant oceanic metrics.

Table 1. Summary of the global simulations performed. NK is the number of vertical layers.

Experiment	**vertical coordinate**	**NK**	**neutral diffusion**	**lateral diffusion**
CTRL-z*	z*	65	entire water column	off
LBD-z*	z*	65	below BLD_{max}	on
CTRL-H	hybrid	41	entire water column	off
LBD-H	hybrid	41	below BLD_{max}	on

4.3.1 Winter-mean surface boundary layer depth

We start by evaluating how the BLD is modified when lateral diffusion is included. We will focus on the winter-mean values because this is when the BLDs are the deepest and the effects of adding lateral diffusion are more pronounced; recall that the lateral diffusion scheme is only acting within the BLD. The differences in BLD in the summer, spring, and fall are significantly smaller and for this reason these are not shown here.

The winter-mean BLDs are shown in Fig. 6. The choice of vertical coordinate has a strong effect in the BLD, with experiments using the z* coordinate (Figs. 6a,b) showing overall shallower global-mean values than experiments using the hybrid coordinate (Figs. 6d,e). However, for either choice of vertical coordinate system, adding lateral diffusion deepens the BLD almost everywhere (Figs. 6c,f). The effect is more pronounced in experiments using the hybrid coordinate (maximum difference is $\sim$ 130 m, Fig. 6f) versus in experiments using z* (maximum difference is $\sim$ 55 m, Fig. 6f).

Differences in the time-averaged diffusion coefficient between experiments with and without lateral diffusion are relatively small and cannot account for the differences in BLD (Appendix A). The deepening of BLDs in experiments with lateral diffusion is more pronounced in regions that tend to have relatively deep winter-mean values, such as in the Labrador, Greenland and Norwegian Seas as well as in the Southern Ocean (Figs. 6c and f).

4.3.2 Potential temperature and salinity bias

To understand how lateral diffusion affects the BLD we now compare time-averaged vertical profiles of potential temperature, salinity and the square of buoyancy frequency

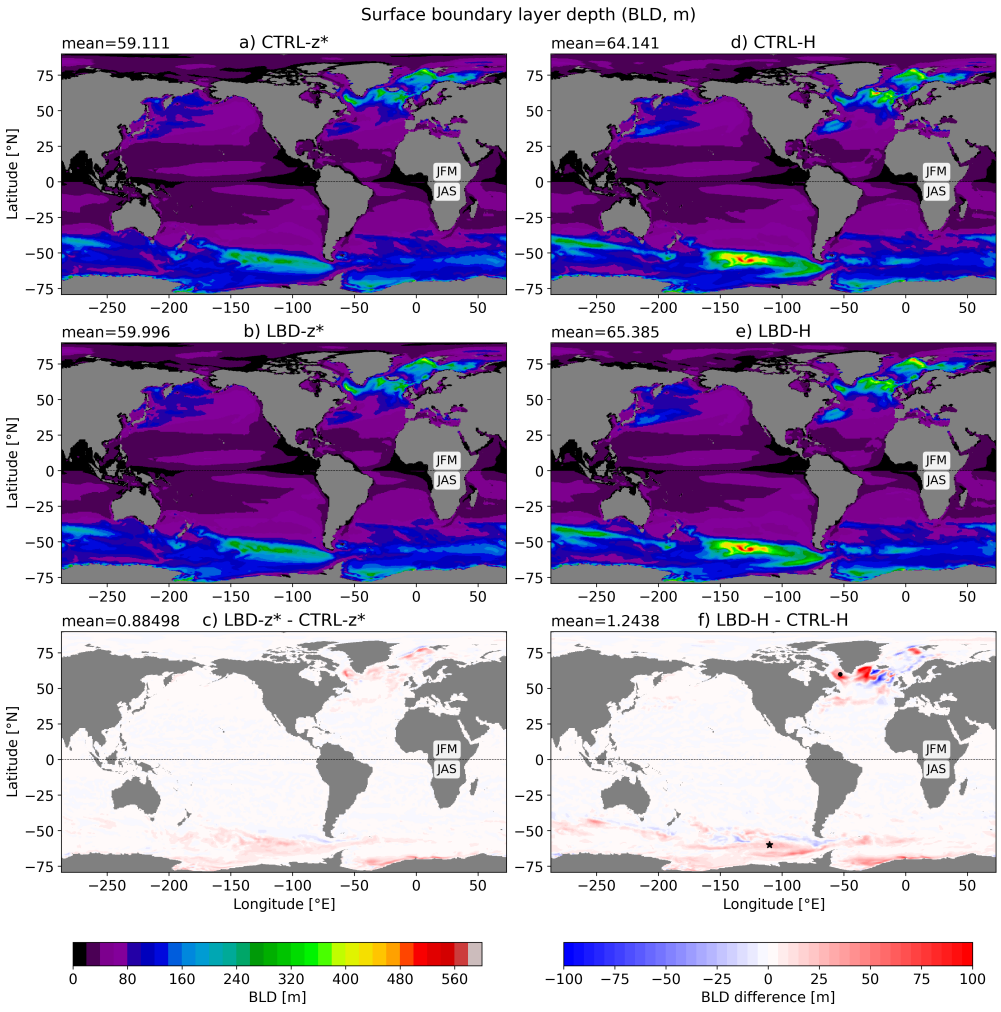

Figure 6. Winter-mean boundary layer depth (BLD, m) averaged over years 28-58. The top and middle panels show results from experiments listed in Table 1: a) CTRL-z*, b) LBD-z*, d) CTRL-H, and e) LBD-H. The bottom panels shown the difference between experiments where the lateral diffusion scheme is enabled and their respective control simulations: c) LBD-z* - CTRL-z*, and f) LBD-H - CTRL-H. Global-mean values are shown at the top of each panel. The black dot and star in panel f are the locations where profiles shown in Figs. 7 and 8 are taken, respectively. JMF = January, February, and March; JAS = July, August, and September.

(computed online as $N^2 = -g\rho_0^{-1}\partial_z\rho$, where g is the gravitational acceleration) from two locations where BLD differences are large: point #1 is located in the Labrador Sea (60.0°N; 53.0°W, see black dot in Fig. 6f) and point #2 is located in the Southern Ocean (60.0°S; 110.0°W, see black star in Fig. 6f).

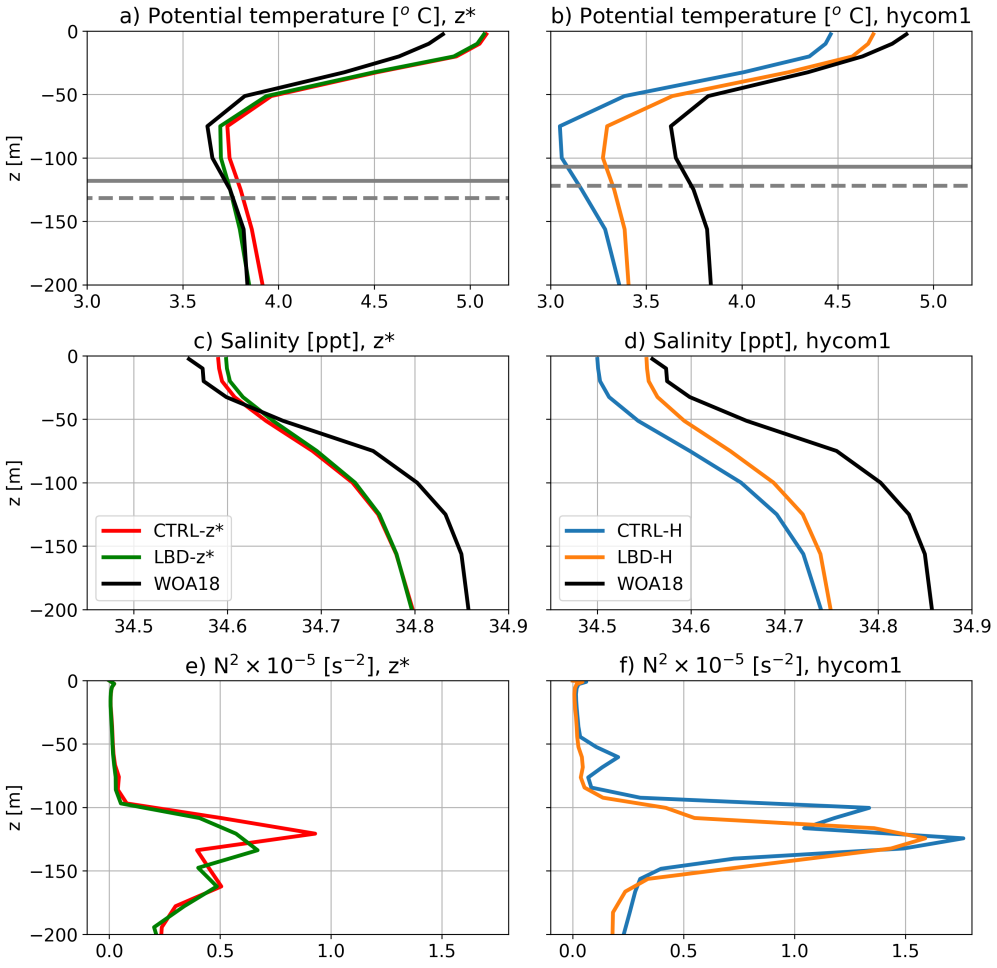

Figure 7. Vertical profiles of potential temperature (θ, panels a and b), salinity (S, panels c and d) and the squared of buoyancy frequency (N^2, panels e and f) taken from a point in the Labrador Sea (60.0°N; 53.0°W, see black dot in Fig. 6f for location) and averaged over years 28-58. Profiles taken from the WOA18 annual mean climatology are shown in black for comparison. The dashed and solid gray horizontal lines in panels a) and b) represent the time-averaged boundary layer depth for cases with and without lateral diffusion, respectively. Only the upper 200 m of the water column is shown.

At point #1, including lateral diffusion leads to a better representation of potential temperature (Fig. 7a,b) and salinity (Fig. 7c,d) profiles when compared to the WOA18 annual mean climatology. This improvement is relatively small in the z* case (Figs. 7a,c), where biases in the control case (CTRL-z*) are relatively small. The improvement is more evident in the hybrid experiment (Fig. 7b,d), because the control case (CTRL-H) displays relatively large biases that are mitigated when lateral diffusion in included. An-

462 other consequence of applying lateral diffusion is the reduction in the vertical stratifi-
463 cation of the upper ocean in certain regions, which occurs in both hybrid and z* cases
464 (Figs. 7e,f).

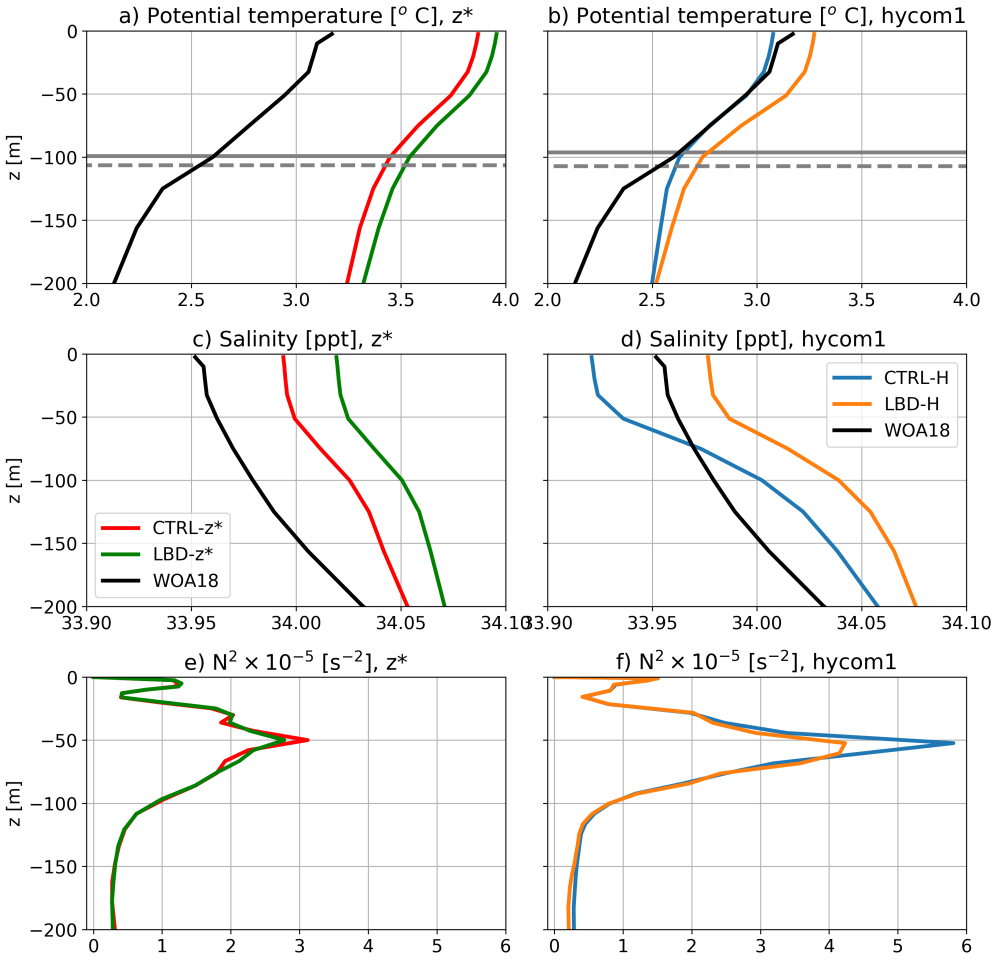

Figure 8. Same as Fig. 7, but for a point located in the Southern Ocean (60.0°S; 110.0°W, see black star in Fig. 6f).

465 Lateral diffusion does not reduce biases everywhere. At point #2, adding lateral
466 diffusion increases the differences in potential temperature (Fig. 8a,b) and salinity (Fig. 8c,d)
467 profiles when compared to the WOA18 annual mean climatology. However, lateral dif-
468 fusion still leads to an overall reduction in the vertical stratification of the upper ocean
469 (Fig. 8e,f). The BLD is a measure of the depth over which turbulent boundary layer ed-
470 dies can penetrate before becoming stable relative to the local velocity and buoyancy.
471 Therefore, the above results suggest that the deepening of the BLDs in experiments with

lateral diffusion enabled (LBD-Z* and LBD-H) is a consequence of the reduction in the vertical stratification.

So far we have seen that from a point-wise perspective adding lateral diffusion can either increase or decrease biases in potential temperature and salinity. To assess the overall effect of lateral diffusion on these tracers, we compare the depth versus time evolution of global biases in potential temperature (Fig. 9) and salinity (Fig. 10) focusing on the upper 1500 m of the water column. CTRL-z* and CTRL-H show an overall warming bias in potential temperature between 100-800 m (Figs. 9a,d). Towards the end of the simulation, the largest bias in experiment CTRL-z* ($\sim$ 0.85 °C, Fig. 9a) is double of the largest bias in experiment CTRL-H ($\sim$ 0.45 °C, Fig. 9d). In both coordinate systems the bias within this depth range is overall reduced by $\sim$ 5% when lateral diffusion is applied (Figs. 9c,f).

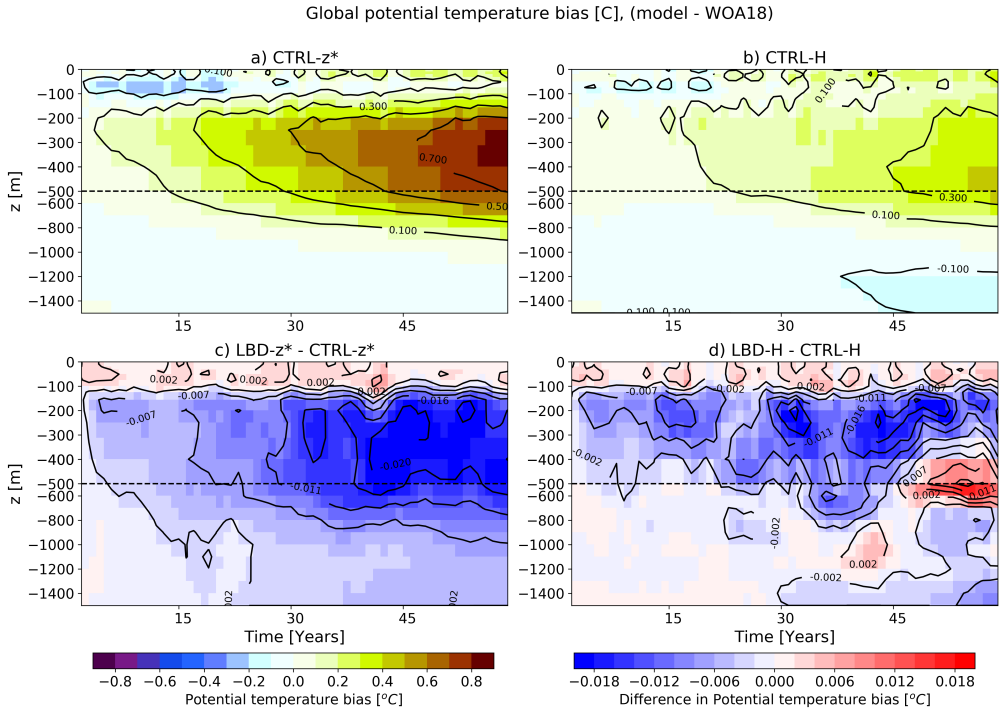

Figure 9. Annual-mean time series of potential temperature bias profiles with respect to the WOA18 annual mean climatology. Results from the control experiments are shown in the top panels: a) CTRL-z* and b) CTRL-H. Differences between experiments where the lateral diffusion scheme is enabled and their respective control simulations are shown in the bottom panels: c) LBD-z* - CTRL-z* and d) LBD-H - CTRL-H. Note the change in the depth scale below 500 m.

In terms of global salinity biases, CTRL-z* and CTRL-H show a fresh bias between 0-300 m (Figs. 10a,d). The overall bias pattern is similar in both cases and the intensity is only slightly stronger in CTRL-z*; minimum values are $\sim$ -0.12 and -0.10 psu in CTRL-z* and CTRL-H, respectively. When lateral diffusion is included, this near surface bias is reduced by $\sim$ 10% in both LBD-Z* and LBD-H (Figs. 10c,f).

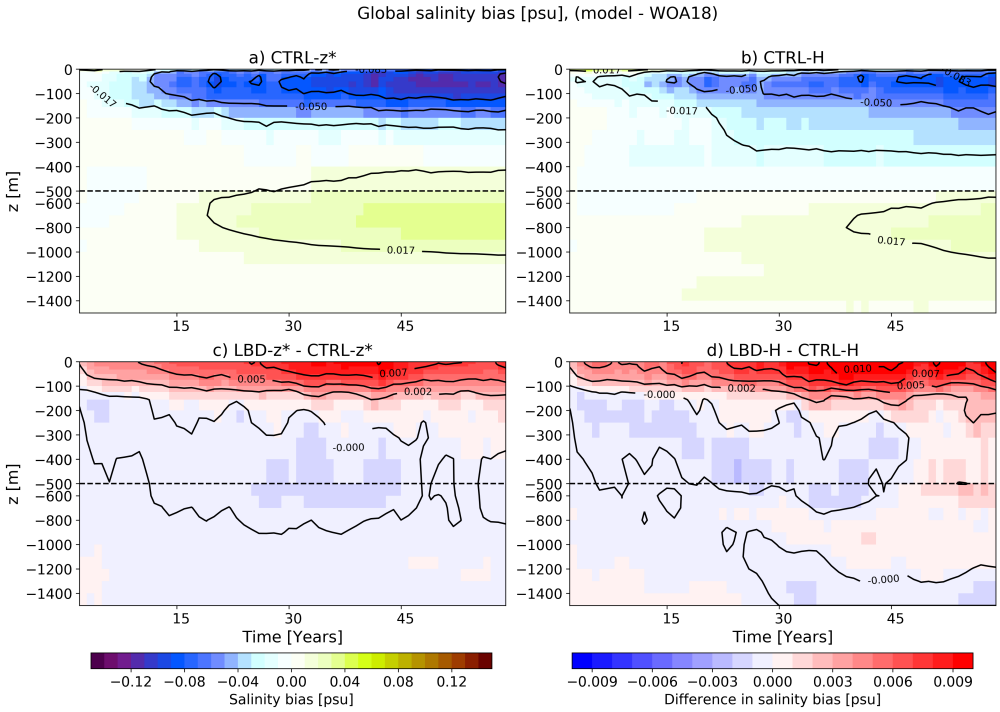

Figure 10. Same as Fig. 9, but for salinity.

4.3.3 Northward global heat transport

Lastly, we explore the impact of the lateral diffusion scheme on the ocean heat transport. Figure 11a shows the total northward global ocean heat transport, which represents the sum of the advection, neutral and lateral diffusion components. Overall, experiments using the hybrid coordinate (CTRL-H and LBD-H) display a slightly stronger poleward heat transport in both Hemispheres, but the difference is relatively small. The effects of the lateral diffusion scheme on the total northward heat transport are not noticeable in Fig. 11a because advection alone accounts for the majority of the total transport almost everywhere (Fig. 11b). Contributions from both neutral (Fig. 11c) and lateral (Fig. 11d) diffusion become notable in the Southern Ocean and in the Western bound-

499 ary current regions of the Northern Hemisphere (not shown). These are the regions that
500 tend to display relatively large eddy diffusivities (Fig. A1) and deep BLDs (Fig. 6). De-
501 spite the fact that lateral diffusion only occurs within the BLD, its contribution is com-
502 parable to that from neutral diffusion regardless of the coordinate system (compare pan-
503 els c and d in Fig. 11). The contribution from lateral diffusion in CTRL-z* and CTRL-
504 H represents at most $\sim 2.5\%$ of the total heat transport.

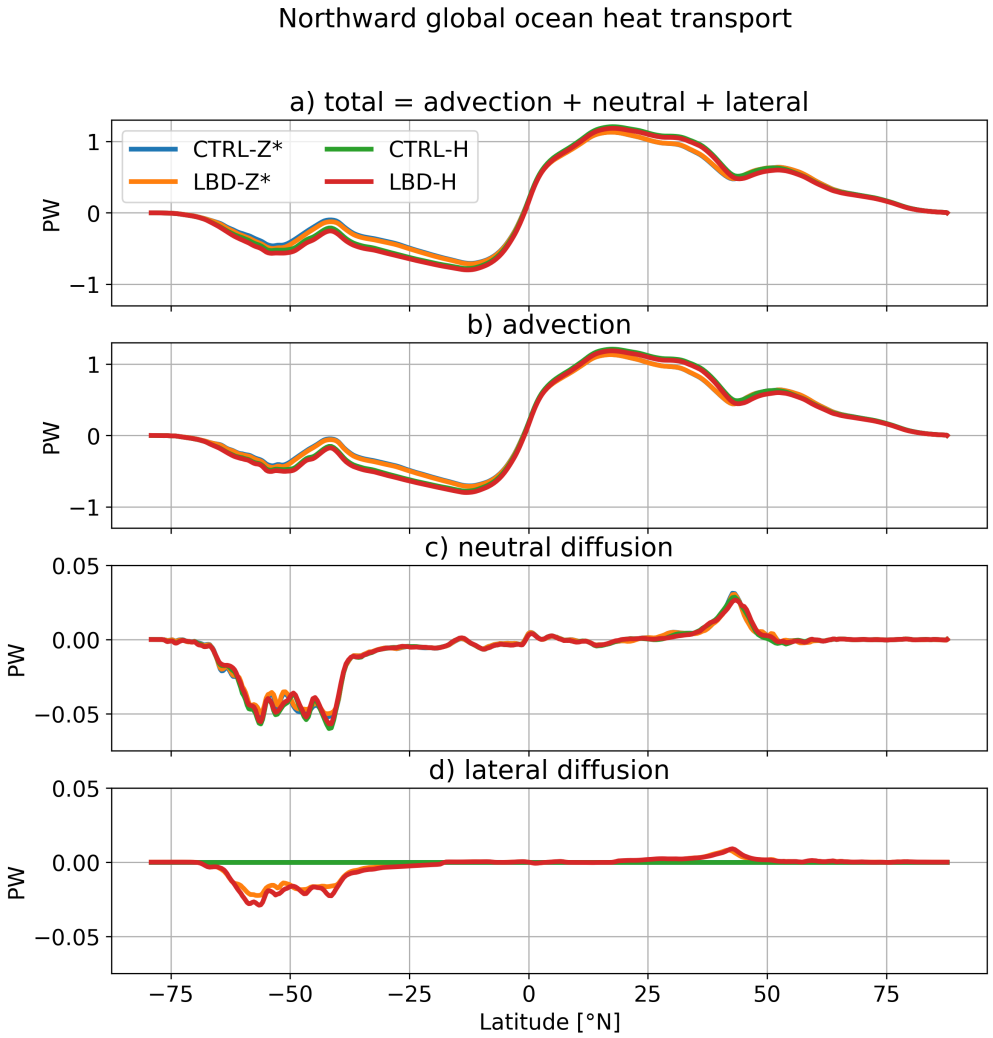

Figure 11. The mean northward global ocean heat transport (PW), total and broken by components, from experiments listed in Table 1. a) total transport (advection + lateral diffusion + neutral diffusion); b) transport due to advection; c) transport due to neutral diffusion; and d) transport due to lateral diffusion. Note the different transport magnitude range in panels c) and d). The mean was computed over years 28-58.

5 Summary and Discussion

We have developed an algorithm for applying lateral eddy diffusion within the surface boundary layer of general vertical coordinate system ocean models. This algorithm uses regridding/remapping techniques to represent tracer profiles in a geopotential vertical coordinate, where lateral fluxes are easily calculated and then remapped back to the native grid. Combined with a neutral diffusion operator appropriate for this class of models (e.g., Shao et al., 2020), the algorithm can be used to represent the transition from neutral to dianeutrally-oriented diffusive fluxes in ocean models. The effect is equivalent to what is achieved via the near-boundary eddy flux parameterization (Ferrari et al., 2008; Danabasoglu et al., 2008) that has been implemented in OGCMs with geopotential vertical coordinates (e.g., Danabasoglu et al., 2012; Griffies et al., 2005; Griffies, 2012; Wang et al., 2014).

The algorithm was implemented in a general vertical coordinate OGCM (MOM6) and we have run a set of forced global experiments using the CESM framework to assess the effects of including lateral diffusion in two different vertical coordinate systems (z* and hybrid). Lateral diffusion leads to a reduction of the vertical stratification within the surface boundary layer of certain regions, which results in an overall deepening of the BLD. This feedback is more (less) pronounced in the hybrid (z*) experiments, where the winter-mean BLD can be on average up to 130 m (55 m) deeper over a 30 year period. While including lateral diffusion does not lead to significant changes in certain climate-relevant metrics, such as northward global heat transport, its inclusion results in an overall reduction of the near-surface global biases in potential temperature and salinity. Its inclusion is also necessary to ensure a physically-consistent suite of mesoscale eddy parameterizations, particularly in the near-surface region where eddy fluxes are known to be large (e.g., Robbins et al., 2000).

We have implemented lateral diffusion within the surface BLD and we defined a transition zone, where we impose a linear decay on the lateral to cover the range between BLDs from two neighbouring cells. Previous studies have defined the transition zone using the concept of a layer being intermittently exposed to strong turbulent mixing (Ferrari et al., 2008; Danabasoglu et al., 2008). However, the effect of including such transition zone in a climate model was negligible (Danabasoglu et al., 2008). We have adopted a different definition for practical reasons because in the absence of this zone, regions where

the BLD can vary significantly between two adjacent grid points (e.g., Labrador Sea) can be left without diffusion in parts of the water column (i.e., the red arrows would be removed in Fig. 2).

The algorithm presented here is both conservative and monotonic and, therefore, it is suitable for use in climate studies. The averaged computational cost of the algorithm is ~ 9 % of the total integration time when employing 3 tracers. This is about half of the cost of the tracer advection scheme and also of the fastest neutral diffusion scheme (method 3) proposed by Shao et al. (2020). The cost is linearly proportional to the number of tracers and, therefore, it can become significantly more expensive when multiple tracers are employed (e.g., in biogeochemical applications). The most expensive part of the algorithm is the construction of the LBD grid (see section 2.1). In the current implementation this step must be repeated for all tracers and this was chosen because a unique LBD grid is constructed for each pair of adjacent water columns, and the number of vertical levels is not known *a priori*. One way to reduce computational cost is by defining a 3-dimensional array with, for example, twice the number of vertical layers in the native grid and use it to store the LBD grid for each pair of grid points. The LBD grid would then be constructed only once per time step, reducing the computational cost of the scheme.

Another limitation of the approach presented here is the fact that neutral diffusion is not included within the transition layer. That is, only the lateral diffusion decays linearly from the top to the bottom of the transition zone. As a consequence of this limitation, it is possible to have a single point in a water column where neither neutral or lateral diffusive fluxes are applied (e.g., Figs. 5e and f). This study focuses only on applying the proper rotation to diffusion in the surface boundary layer and introducing the concept of achieving this rotation via regridding/remapping, so this issue is not rectified here. A proper conciliation between the neutral and lateral diffusion schemes is the subject of ongoing research as part of the Ocean Transport and Eddy Energy Climate Process Team (https://ocean-eddy-cpt.github.io/), and will be presented in forthcoming work.

Appendix A Mesoscale eddy diffusivities

Because the mesoscale eddy diffusivities (κ) are derived from a prognostic equation for the mesoscale eddy kinetic energy, it is important to check how adding lateral diffusion within different vertical coordinates influences this field. The time-averaged κ is shown in Fig. A1. The overall pattern of κ is very similar in all experiments, with larger values occurring in the Southern Ocean and along western boundary currents. Experiments with a hybrid coordinate (Figs. A1d,e) have slightly larger κ, both globally-averaged and in the Southern Ocean, when compared to the z* cases (Figs. A1a,b). From a globally-averaged perspective, adding lateral diffusion does not affect κ. However, locally, the differences in κ can be up to order 10 %, regardless of the coordinate system (Figs. A1c,f).

Acknowledgments

We thank Keith Lindsay for suggesting the diffusive flux limiter described in section 2. The CESM project is supported primarily by the National Science Foundation (NSF). This material is based upon work supported by NCAR, which is a major facility sponsored by NSF under cooperative agreement 1852977. Computing and data storage resources, including the Cheyenne supercomputer (doi:10.5065/D6RX99HX), were provided by the Computational and Information Systems Laboratory at NCAR. G.M.M and S.D.B. are supported by NSF OCE 1912420.

The World Ocean Atlas 2018 is available at (https://www.ncei.noaa.gov/access/world-ocean-atlas-2018/, last access: December 2020).

Source code for the idealized and global models, experiments configurations, main results, and analysis/plotting scripts are available at https://doi.org/10.5281/zenodo.4701599

References

Adcroft, A., Anderson, W., Balaji, V., Blanton, C., Bushuk, M., Dufour, C. O., ... others (2019). The gfdl global ocean and sea ice model om4. 0: Model description and simulation features. *J. Adv. Model. Earth Syst.*, *11*(10), 3167–3211.

Adcroft, A., & Campin, J.-M. (2004). Rescaled height coordinates for accurate representation of free-surface flows in ocean circulation models. *Ocean Modell.*, *7*(3-4), 269–284.

Bachman, S. D., Fox-Kemper, B., & Bryan, F. O. (2020). A diagnosis of anisotropic

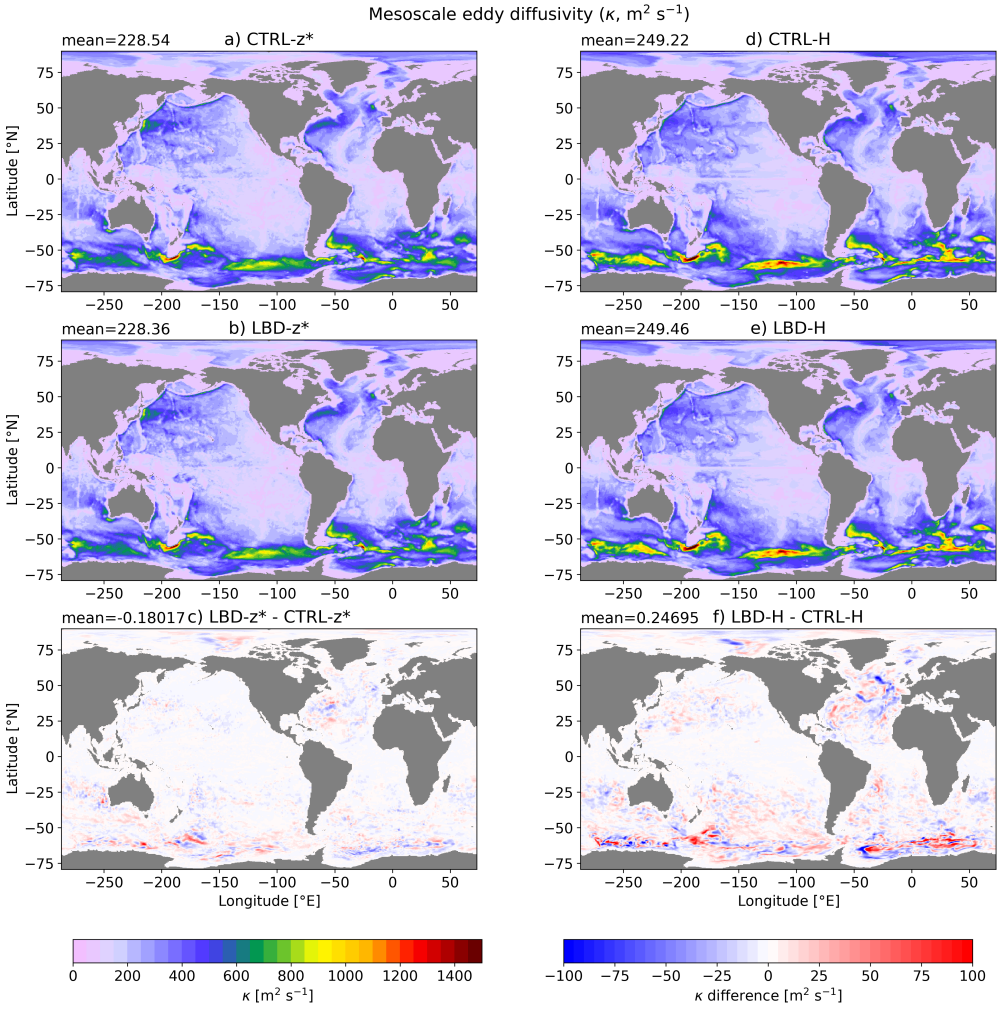

Figure A1. Mesoscale eddy diffusivity averaged over years 28-58 (κ, m^2 s^{-1}). The top and middle panels show results from experiments listed in Table 1: a) CTRL-z*, b) LBD-z*, d) CTRL-H, and e) LBD-H. The bottom panels shown the difference between experiments where the lateral diffusion scheme is enabled and their respective control: c) LBD-z* - CTRL-z*, and f) LBD-H - CTRL-H.

eddy diffusion from a high-resolution global ocean model. *J. Adv. Model. Earth Syst.*, *12*(2), e2019MS001904.

Bailey, D., DuVivier, A., Holland, M., Hunke, E., Lipscomb, B., Briegleb, B., ... Schramm, J. (2018). *CESM CICE5 users guide* (Tech. Rep.). Tech. rep.

Bleck, R. (2002). An oceanic general circulation model framed in hybrid isopycnic-cartesian coordinates. *Ocean Modell.*, *4*(1), 55–88.

Danabasoglu, G., Bates, S., Briegleb, B. P., Jayne, S. R., Jochum, M., Large, W. G.,

... Yeager, S. G. (2012). The CCSM4 ocean component. *J. Climate*, *25*(5), 1361–1389.

Danabasoglu, G., Ferrari, R., & McWilliams, J. C. (2008). Sensitivity of an ocean general circulation model to a parameterization of near-surface eddy fluxes. *J. Climate*, *21*(6), 1192–1208.

Danabasoglu, G., Lamarque, J.-F., Bacmeister, J., Bailey, D., DuVivier, A., Edwards, J., ... others (2020). The Community Earth System Model version 2 (CESM2). *J. Adv. Model. Earth Syst.*, *12*(2), e2019MS001916.

Danabasoglu, G., McWilliams, J. C., & Gent, P. R. (1994). The role of mesoscale tracer transports in the global ocean circulation. *Science*, *264*(5162), 1123–1126.

Farneti, R., Delworth, T. L., Rosati, A. J., Griffies, S. M., & Zeng, F. (2010). The role of mesoscale eddies in the rectification of the Southern Ocean response to climate change. *J. Phys. Oceanogr.*, *40*(7), 1539–1557.

Ferrari, R., Griffies, S. M., Nurser, A. G., & Vallis, G. K. (2010). A boundary-value problem for the parameterized mesoscale eddy transport. *Ocean Modell.*, *32*(3-4), 143–156.

Ferrari, R., McWilliams, J. C., Canuto, V. M., & Dubovikov, M. (2008). Parameterization of eddy fluxes near oceanic boundaries. *J. Climate*, *21*(12), 2770–2789.

Fox-Kemper, B., Danabasoglu, G., Ferrari, R., Griffies, S., Hallberg, R., Holland, M., ... Samuels, B. (2011). Parameterization of mixed layer eddies. iii: Implementation and impact in global ocean climate simulations. *Ocean Modell.*, *39*(1-2), 61–78.

Fox-Kemper, B., Ferrari, R., & Hallberg, R. (2008). Parameterization of mixed layer eddies. Part I: Theory and diagnosis. *J. Phys. Oceanogr.*, *38*(6), 1145–1165.

Gent, P. R., & McWilliams, J. C. (1990). Isopycnal mixing in ocean circulation models. *J. Phys. Oceanogr.*, *20*(1), 150–155.

Gent, P. R., Willebrand, J., McDougall, T. J., & McWilliams, J. C. (1995). Parameterizing eddy-induced tracer transports in ocean circulation models. *J. Phys. Oceanogr.*, *25*(4), 463–474.

Gnanadesikan, A., Griffies, S. M., & Samuels, B. L. (2007). Effects in a climate model of slope tapering in neutral physics schemes. *Ocean Modell.*, *16*(1-2), 1–16.

Griffies, S. M. (1998). The Gent–McWilliams Skew Flux. *J. Phys. Oceanogr.*, *28*(5), 831–841.

Griffies, S. M. (2012). *Elements of the modular ocean model (MOM)* (Vol. 7; Tech. Rep. No. 620). Geophysical Fluid Dynamics Laboratory.

Griffies, S. M., Gnanadesikan, A., Dixon, K. W., Dunne, J., Gerdes, R., Harrison, M. J., ... others (2005). Formulation of an ocean model for global climate simulations. *Ocean Science*, *1*(1), 45–79.

Griffies, S. M., Winton, M., Anderson, W. G., Benson, R., Delworth, T. L., Dufour, C. O., ... others (2015). Impacts on ocean heat from transient mesoscale eddies in a hierarchy of climate models. *J. Climate*, *28*(3), 952–977.

Gula, J., Molemaker, M. J., & McWilliams, J. C. (2014). Submesoscale cold filaments in the Gulf Stream. *J. Phys. Oceanogr.*, *44*(10), 2617–2643.

Hallberg, R., & Gnanadesikan, A. (2006). The role of eddies in determining the structure and response of the wind-driven Southern Hemisphere overturning: Results from the Modeling Eddies in the Southern Ocean (MESO) project. *J. Phys. Oceanogr.*, *36*(12), 2232–2252.

Holloway, G. (1997). Eddy transport of thickness and momentum in layer and level models. *J. Phys. Oceanogr.*, *27*(6), 1153–1157.

Hoskins, B. J. (1982). The mathematical theory of frontogenesis. *Annual review of fluid mechanics*, *14*(1), 131–151.

Jansen, M. F., Adcroft, A. J., Hallberg, R., & Held, I. M. (2015). Parameterization of eddy fluxes based on a mesoscale energy budget. *Ocean Modell.*, *92*, 28–41.

Large, W. G., McWilliams, J. C., & Doney, S. C. (1994). Oceanic vertical mixing: A review and a model with a nonlocal boundary layer parameterization. *Reviews of Geophysics*, *32*(4), 363–403.

Locarnini, M., Mishonov, A., Baranova, O., Boyer, T., Zweng, M., Garcia, H., ... others (2018). *World ocean atlas 2018, volume 1: Temperature* (Vol. 81; Tech. Rep.). NOAA Atlas NESDIS.

Marshall, D. P., Ambaum, M. H., Maddison, J. R., Munday, D. R., & Novak, L. (2017). Eddy saturation and frictional control of the Antarctic Circumpolar Current. *Geophys. Res. Lett.*, *44*(1), 286–292.

Marshall, D. P., Maddison, J. R., & Berloff, P. S. (2012). A framework for parameterizing eddy potential vorticity fluxes. *J. Phys. Oceanogr.*, *42*(4), 539–557.

669 Petersen, M. R., Asay-Davis, X. S., Jacobsen, D. W., Maltrud, M. E., Ringler,
670 T. D., Van Roekel, L., ... Wolfram Jr, P. J. (2018). *MPAS-Ocean Model*
671 *User's Guide Version 6.0* (Tech. Rep.). Los Alamos National Lab.(LANL), Los
672 Alamos, NM (United States).

673 Redi, M. H. (1982). Oceanic isopycnal mixing by coordinate rotation. *J. Phys.*
674 *Oceanogr.*, *12*(10), 1154–1158.

675 Robbins, P. E., Price, J. F., Owens, W. B., & Jenkins, W. J. (2000). The impor-
676 tance of lateral diffusion for the ventilation of the lower thermocline in the
677 subtropical North Atlantic. *J. Phys. Oceanogr.*, *30*(1), 67–89.

678 Shao, A. E., Adcroft, A., Hallberg, R., & Griffies, S. M. (2020). A General-
679 Coordinate, Nonlocal Neutral Diffusion Operator. *J. Adv. Model. Earth Syst.*,
680 *12*(12), e2019MS001992.

681 Simmons, H. L., Jayne, S. R., Laurent, L. C. S., & Weaver, A. J. (2004). Tidally
682 driven mixing in a numerical model of the ocean general circulation. *Ocean*
683 *Modell.*, *6*(3-4), 245–263.

684 Smith, R. D. (1999). The primitive equations in the stochastic theory of adiabatic
685 stratified turbulence. *J. Phys. Oceanogr.*, *29*(8), 1865–1880.

686 Solomon, H. (1971). On the representation of isentropic mixing in ocean circulation
687 models. *J. Phys. Oceanogr.*, *1*(3), 233–234.

688 Stacey, M. W., Pond, S., & Nowak, Z. P. (1995). A numerical model of the circu-
689 lation in Knight Inlet, British Columbia, Canada. *J. Phys. Oceanogr.*, *25*(6),
690 1037–1062.

691 Taylor, J. R., & Ferrari, R. (2010). Buoyancy and wind-driven convection at mixed
692 layer density fronts. *J. Phys. Oceanogr.*, *40*(6), 1222–1242.

693 Thomas, L. N. (2005). Destruction of potential vorticity by winds. *J. Phys.*
694 *Oceanogr.*, *35*(12), 2457–2466.

695 Thomas, L. N., & Ferrari, R. (2008). Friction, frontogenesis, and the stratification of
696 the surface mixed layer. *J. Phys. Oceanogr.*, *38*(11), 2501–2518.

697 Tréguier, A.-M., Held, I. M., & Larichev, V. (1997). Parameterization of quasi-
698 geostrophic eddies in primitive equation ocean models. *J. Phys. Oceanogr.*,
699 *27*(4), 567–580.

700 Tsujino, H., Urakawa, L. S., Griffies, S. M., Danabasoglu, G., Adcroft, A. J., Ama-
701 ral, A. E., ... others (2020). Evaluation of global ocean–sea-ice model simula-

tions based on the experimental protocols of the Ocean Model Intercomparison Project phase 2 (OMIP-2). *Geosci. Model Dev.*, *13*(8), 3643–3708.

Tsujino, H., Urakawa, S., Nakano, H., Small, R. J., Kim, W. M., Yeager, S. G., ... others (2018). JRA-55 based surface dataset for driving ocean–sea-ice models (JRA55-do). *Ocean Modell.*, *130*, 79–139.

Urakawa, L. S., Tsujino, H., Nakano, H., Sakamoto, K., Yamanaka, G., & Toyoda, T. (2020). The sensitivity of a depth-coordinate model to diapycnal mixing induced by practical implementations of the isopycnal tracer diffusion scheme. *Ocean Modell.*, *154*, 101693.

Wang, Q., Danilov, S., Sidorenko, D., Timmermann, R., Wekerle, C., Wang, X., ... Schröter, J. (2014). The Finite Element Sea Ice-Ocean Model (FESOM) v. 1.4: formulation of an ocean general circulation model. *Geosci. Model Dev.*, *7*(2), 663–693.

White, L., & Adcroft, A. (2008). A high-order finite volume remapping scheme for nonuniform grids: The piecewise quartic method (PQM). *J. Comp. Phys.*, *227*(15), 7394–7422.

White, L., Adcroft, A., & Hallberg, R. (2009). High-order regridding–remapping schemes for continuous isopycnal and generalized coordinates in ocean models. *J. Comp. Phys.*, *228*(23), 8665–8692.

Wright, D. G. (1997). An equation of state for use in ocean models: Eckart's formula revisited. *J. Atmos. Ocean. Technol.*, *14*(3), 735–740.

Zweng, M., Seidov, D., Boyer, T., Locarnini, M., Garcia, H., Mishonov, A., ... others (2019). *World ocean atlas 2018, volume 2: Salinity* (Vol. 82; Tech. Rep.). NOAA Atlas NESDIS.